Computers and Concrete, Vol. 4, No. 3 (2007) 221-241
DOI: http://dx.doi.org/10.12989/cac.2007.4.3.221

Numerical simulation of fracture and damage behaviour of concrete at different ages

Nanguo Jin, Ye Tian and Xianyu Jin†

Department of Civil Engineering, Zhejiang University, Hangzhou 310027, China
(Received September 16, 2006, Accepted June 29, 2007)

Abstract. Based on the experiment results, the damage and fracture behavior of concrete at the ages of 1d, 2d, 7d and 28d, in three-point bending and uniaxial tensile tests, were simulated with a finite element program, ABAQUS. The critical stress intensity factor K_{IC}^{s} and the critical crack tip opening displacement ($CTOD_C$) of concrete were calculated with effective-elastic crack approach for the three-point bending test of grade C30 concrete. Based on the crack band model, a bilinear strain-softening curve was derived to simulate the LOAD-CMOD curves and LOAD-Displacement curves. In numerical analysis of the uniaxial tension test of concrete of grade C40, the damage and fracture mechanics were combined. The smeared cracking model coupling with damaged variable was adopted to evaluate the onset and development of microcracking of uniaxial tensile specimen. The uniaxial tension test was simulated by invoking the damage plastic model which took both damage and plasticity as inner variables with user subroutines. All the numerical simulated results show good agreement with the experimental results.

Keywords: concrete; ABAQUS; three-point bending test; uniaxial tension test; damage; fracture.

1. Introduction

The damage and fracture behavior of concrete at different ages have attracted a lot of attention in last a few decades.

In 2002, Z. P. Bazant reviewed the existing fracture models for concrete and the testing methods for fracture energy and other fracture characteristic (Bazant 2002). He related the fracture energy of concrete, as well as other fracture parameters such as the effective length of the fracture process zone, critical crack-tip opening displacement and the fracture toughness with the standard compression strength, maximum aggregate size, water-cement ratio, and aggregate type of concrete. Jin, *et al.* (2005) had ever applied two-parameter model (TPM) to investigate the fracture properties of normal concrete and high strength concrete at early ages. Jin, *et al.* (2004) also studied K_{IC}^{s} and $CTOD_C$ as well as microstructure of early-age concrete. Li and Jin (2004) discussed the relationship between porosity and fracture parameter of young concrete. Niu, *et al.* (1995) analyzed the thermomechanical damage of early-age concrete. Kim (2004) investigated the fracture characteristics such as critical crack tip opening displacement, critical stress intensity factor, fracture energy and obtained bilinear softening curve as an input data for finite element analysis of concrete at early ages.

† Professor, Corresponding Author, E-mail address: xianyu@zju.edu.cn

These experiment results and established models of the researches have provided good base for the numerical investigation on fracture and damage properties of concrete at different ages. Stergaard *et al.* (2004) developed a new inverse analysis algorithm for the extraction of the stress-crack opening relationships. Hanson and Ingraffea (2003) developed the models to predict crack growth in materials such as concrete with tension softening behavior. Lackner, *et al.* (2004) developed and applied a three-dimensional model to simulate the early-age cracking of concrete. Schutter and Vuylsteke (2004) utilize finite element method to simulate the evolving temperature fields and damage at any time during hardening for concrete. However, most previous investigations limited research merely to damage or fracture properties neglecting the internal relationship of damage and fracture behavior of concrete at different ages. Moreover, there was no systematic study on numerical analysis of damage and fracture behavior of concrete at different ages with the finite element method.

The purpose of this study is to investigate the material fracture and damage behavior of concrete at ages of 1d, 2d, 7d and 28d, and further clarify the failure process of concrete at different ages. In this study, the three-point bending and uniaxial tensile tests of concrete were simulated. By applying the effective-elastic crack approach, the critical stress intensity factor, K_{IC}^{s}, and critical crack tip opening displacement ($CTOD_C$) of concrete were calculated. By utilizing the crack band model and a bilinear strain-softening curve with the parameters determined from the three-point bending tests, the global behavior under the progress of damage and fracture, the load-CMOD and load-displacement curve, were simulated and compared with the curves obtained by experiment at different ages. A good agreement had been found between the simulated and experimented results. The smeared cracking model with damage parameters was adopted to simulate the onset and development of the cracking of concrete under uniaxial tensile. The numerical results showed that such a simulation could predict the global behavior of load-displacement of concrete at different ages well.

2. Materials and mix proportions

Two concrete mix proportions utilized in this study are listed in Table 1. The detail information of raw materials is given as follows:

- Cement used in this study was ASTM Type I Portland cement (or ordinary Portland cement in the British Standards Institution), with relative density of 3.15 and fineness of 385 m^2/kg.
- The coarse aggregate used was crushed limestone with a maximum size of 10 mm, and relative density of 2.57.
- The fine aggregate used was natural river sand with a fineness modulus of 2.3, and relative density of 2.66.

Table 1 Mix proportions

Mix	W/C	Cement	Coarse aggregate	Fine aggregate
C30	0.55	1.0	2.7	2.0
C40	0.50	1.0	1.5	2.4

3. There-point bending test

3.1. Experiment program

At least four beams were tested in each group, and total 4 groups of specimens were tested at 4 different ages. The specimen size was 75 mm × 150 mm × 750 mm. The depth of the notch, a_0, was 50 mm, and the width of the notch, 3 mm. The span length, S (the clear distance between two supports), was 600 mm. All the specimens were demoulded one day after casting, and then cured under the temperature of (23 ± 2)°C and the relative humidity of 100%. A typical load-CMOD curve and a sketch of the specimen are shown in Fig. 1. As shown in Fig. 2, the bending tests were conducted with Materials Testing System (MTS810) with a maximum loading capacity of 250 kN. The tests were controlled by the crack mouth opening displacement (CMOD) as the feedback to obtain stabilized post peak response.

3.2. Two-parameter model (TPM)

In this model, the critical stress intensity K_{IC}^{s}, the critical crack tip opening displacement $\mathrm{CTOD_C}$ and the modulus of elasticity can be calculated as follows (Jenq and Shah 1985):

$$E = 6Sa_0V(\alpha_0)/(C_iD^2B) \tag{1}$$

where S, a_0 and D are shown in Fig. 1; $\alpha_0 = (a_0 + H_0)/(D + H_0)$ and H_0 is the thickness of the clamp; $V(\alpha_0)$ is the shape function about α_0, $V(\alpha_0) = 0.76 - 2.28\alpha_0 + 3.87\alpha_0^2 - 2.02\alpha_0^3 + 0.66/(1-\alpha_0)^2$; B is the width of the specimen; C_i is the initial flexibility.

Take E into Eq.(2) and the critical effective crack length, a_e, can be determined.

$$a_e = EC_uD^2B/(6SV(\alpha_e)) \tag{2}$$

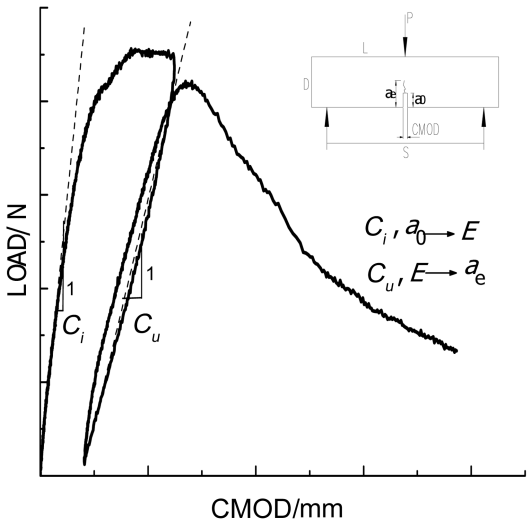

Fig. 1 Typical load-CMOD curve

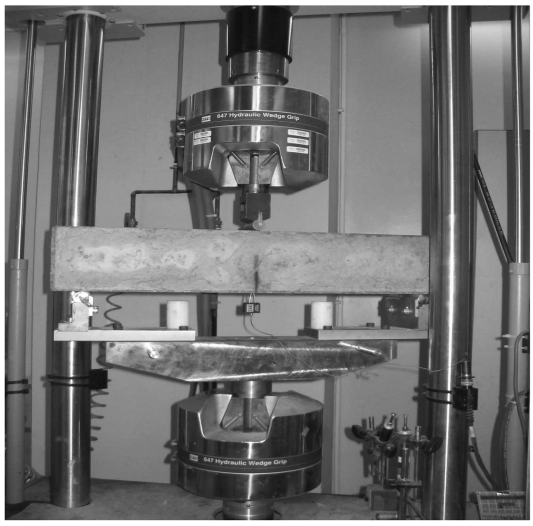

Fig. 2 Bending test setup

Table 2 TPM results for concrete of C30

Ages (d)	K_{IC}^{S} (MPa · m$^{0.5}$)	CTOD$_C$ (mm)	$f_c^{'}$ (Mpa)
1 d	0.415	0.0109	10.46
2 d	0.707	0.0146	15.30
7 d	0.977	0.0143	25.66
28d	1.263	0.0159	35.97

More details about this test can be found in the literature (Jin, *et al*. 2005).

where $\alpha_e = (a_e + H_0)/(D + H_0)$; $V(\alpha_e)$ is the same shape function as $V(\alpha_0)$ in which α_0 is replaced by α_e; C_u is the unloading flexibility.

$$K_{IC}^{s} = \frac{3(P_{\max} + 0.5WS/L)S}{2D^2B}\sqrt{\pi a_e}F(\alpha) \tag{3}$$

where $P_{\max}$ is the ultimate load; $\alpha = a_e/D$; W is the weight of the beam; $F(\alpha)$ is the shape function about α, $F(\alpha)=[1.99-\alpha(1-\alpha)(2.15\text{-}3.93\alpha+2.7\alpha^2)]/[\sqrt{\pi}(1+2\alpha)(1-\alpha)^{3/2}$; L is the length of the beam.

$$CTOD_C = \frac{6(P_{\max} + 0.5WS/L)Sa_e}{D^2BE}V(\alpha)\{(1-\beta)^2 + (-1.14\alpha + 1.081)(\beta - \beta^2)\}^{1/2} \tag{4}$$

where $\beta = a_0/a_e$.

The test results are listed in Table 2.

3.3. Numerical analysis

3.3.1. The finite element model

The crack band model proposed by Bazant (2002) is utilized for numerical analysis of concrete under three point bending. In the case of plane stress, when two cracks occur on a Gaussian point of an element, along the cracking direction, the incremental form stress-strain relationship can be expressed as:

$$\begin{Bmatrix} \Delta\sigma_{nn} \\ \Delta\sigma_{tt} \\ \Delta\sigma_{nt} \end{Bmatrix} = \begin{bmatrix} k_{soft,1}E_0 & 0 & 0 \\ 0 & k_{soft,2}E_0 & 0 \\ 0 & 0 & \varphi G_0 \end{bmatrix} \begin{Bmatrix} \Delta\varepsilon_{nn} \\ \Delta\varepsilon_{tt} \\ \Delta\varepsilon_{nt} \end{Bmatrix} \tag{5}$$

where σ_{nn} and ε_{nn} are the positive stress and strain of crack 1 respectively, while σ_{tt} and ε_{tt} are respectively the positive stress and strain of crack 2. σ_{nt} and ε_{nt} are the shear stress and strain. E_0 is the initial modulus of elasticity; G_0 is the initial modulus of shear; $k_{soft,1}$ and $k_{soft,2}$ are respectively the tension crack softening coefficient of crack 1 and crack 2; φ is shear transfer factor and it reveals the interlocking action between the surfaces of the crack. Because the deformation mode for crack propagation and fracture, in this research, is opening mode, so post-shear effect can be neglected.

In smeared crack model, the conception of band width in this model is equal to the characteristic length of the element in ABAQUS, which is dependent of the element type. For beam and truss elements, it is the distance between Gaussian points. For shell and plane elements, it is the square

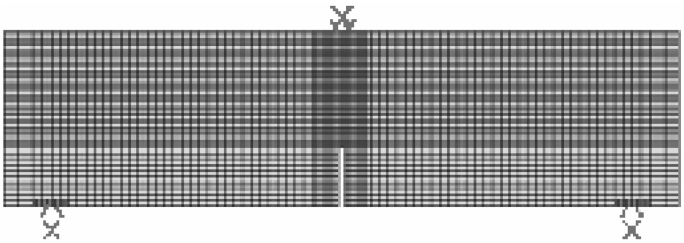

Fig. 3 FEM mesh of three-point bending beam

root of the distance between Gaussian points. While for solid elements, it is the cube root of the distance between Gaussian points. CPS4R (plane stress 4-node simplified integral element) in ABAQUS element family was adopted in this simulation, the sum of the elements and nodes were 3 702 and 3 905 respectively. A modified Riks iterative method was applied to find the softening curve. Fine meshing was adopted within the crack band and supports. The supports and the loading bar were simulated by analytical rigid bodies. The detailed meshing partitions are shown in Fig. 3.

3.3.2. Bilinear tension softening curve

It is well known that there exists a fracture process zone in front of the crack tip, which arouses a phenomenon termed as tension softening. This characteristic plays a very important role on finding the ultimate load and the descending curve.

The primitive work was completed by Hillerborg (1976). He suggested an exponential decay softening curve with the separate displacement, w, independent variable (see Fig. 4). Thereafter, based on large amounts of experiments, Petersson (1981) gave a bilinear softening curve, as shown in Fig 5. Subsequent experiments and numerical analysis indicated that it was adequate for bilinear curve to describe this softening phenomenon.

The stress value at the slope transition is usually taken as $0.15f_t$~$0.33f_t$, and the area under the stress-displacement curve represents the required energy to develop an unit area crack, denoted as G_F (N/m). G_f represents the area under the initial slope. Planas, *et al.* (1997) pointed out that it was that determined the ultimate load. The value of G_f in Two-Parameter Model (TPM) is equal to the critical strain energy release rate, denoted as G^s_{IC}. Once the stress at slope transition is determined, with G_F and G_f, the shape of the bilinear tension softening curve can be gained. Assuming the stress

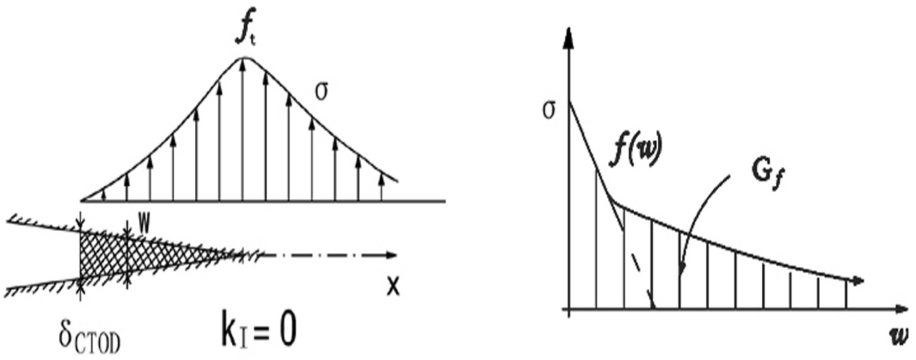

Fig. 4 Stress distribution of FPZ and soften curve (after reaching ft should be a constant!)

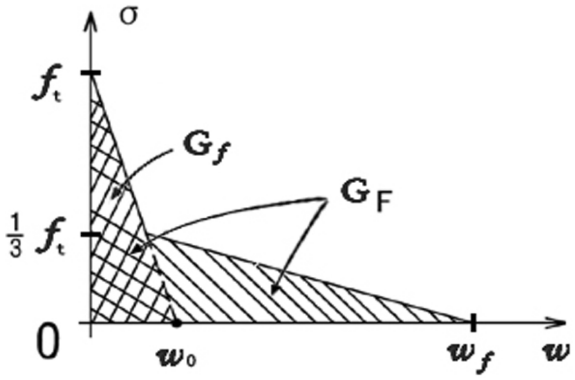

Fig. 5 Bilinear tension soften stress-displacement curve

at slope transition is ψf_t, two equations below can be derived from area calculations:

$$W_0 = \frac{2G_f}{f_t} \tag{6}$$

$$W_f = \frac{2}{\psi f_t}[G_F - (1-\psi)G_f] \tag{7}$$

By trial and errors, Petersson's suggestion of $\psi = 1/3$ is adopted. To get an approximation of G_F, the K_{IC}^s,directly obtained from three point bending test, is used.

First, K_{IC}^s is determined by the equation below:

$$G_{IC}^s = K_{IC}^{s\,2} / E \tag{8}$$

Then, based on the conclusions proposed by Planas (1992) and Guinea (1994), an approximate equation of G_F affirmed by Bazant, *et al*. (2002) can be obtained as:

$$G_F \approx 2.5 G_f = 2.5 {}_{IC}^{s} \tag{9}$$

This relationship had been taken as the optimal choice generalized from 238 series of tests in different labs around the world.

In general, we can write:

$$G_F = k G_{IC}^s \tag{10}$$

where $k \geq 2$.

Normally, the ratio of tension strength to compression strength of concrete is 1/12~1/10, from which W_0 and W_f can be determined. W_0 and W_f can be taken as the length incremental of crack band width, h, the characteristic element length in ABAQUS. Then Eqs. (6) and (7) can be rewritten as:

$$\varepsilon_0 = \frac{2G_f}{f_t h} \tag{11}$$

$$\varepsilon_f = \frac{2}{\psi f_t h}[G_F - (1-\psi)G_f] \tag{12}$$

3.3.3. Numerical analysis

Taking three-point bending concrete beam of 28d for example, its cracking deformation and stress distribution in the whole failure process are shown as follows:

It can be seen from Figs. 6~8 that the opening displacement gradually increases with the increasing load, the maximum tension stress is developing upwards into the ligament of beam along the notch. For the existence of the fracture process zone, the tension stress is not rapidly decreasing to zero, that is, a fraction of stress still remains. Taking out the first cracking element above the notch, a stress-strain curve of integral point is shown in Fig. 9.

From the numerical results of ABAQUS, the LOAD-CMOD curves at ages of 1, 2, 7, 28 days can be derived as Fig. 10 shows:

As shown in Fig. 10, the numerical results match up with the experiment results in the ascending segment of the curves. However, as to the descending segment, it has not a very good agreement for following reasons:

1. Because of the unloading process occurring in the TPM test, energy loss cannot be avoided;
2. The crack band theory assumes that G_F can only be dissipated in crack band zone, while all deformations out of this band are elastic, which cannot dissipate the fracture energy. However, it can be clearly seen from Figs. 6~8 that there do exist some plastic deformations near the supports, which by all means dissipate the fracture energy.

From the comparisons of the numerical and experimental results, it is found that the average error is merely about 3%, which indicates that the calculations of G_f that determines the ultimate load is relatively exact.

Comparisons of LOAD-CMOD curves and LOAD-Displacement curves at different ages are

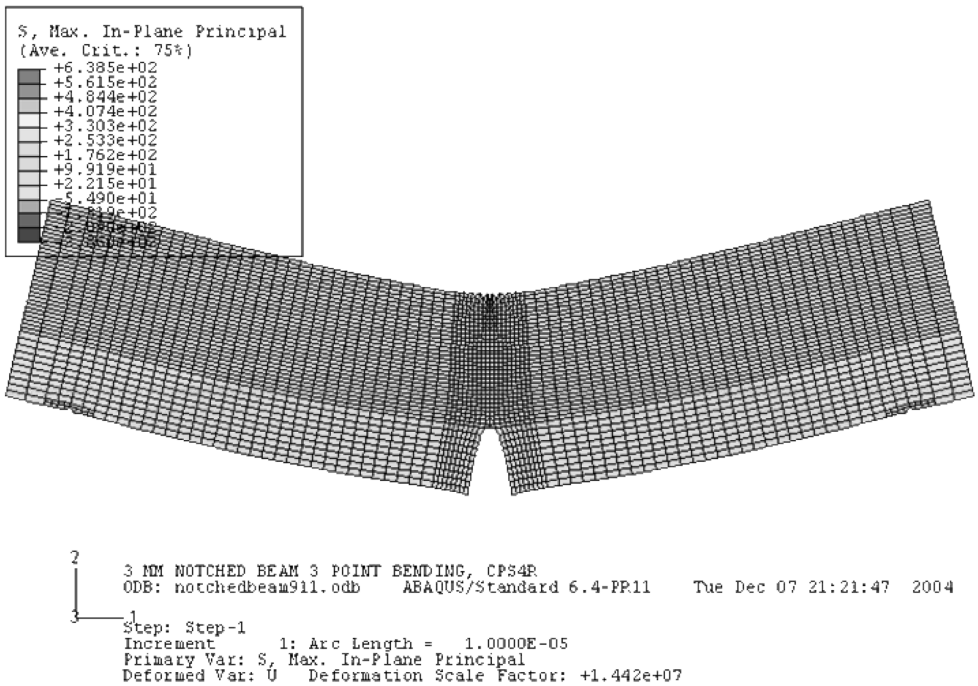

Fig. 6 Initial cracking deformations and distribution of the maximum principle

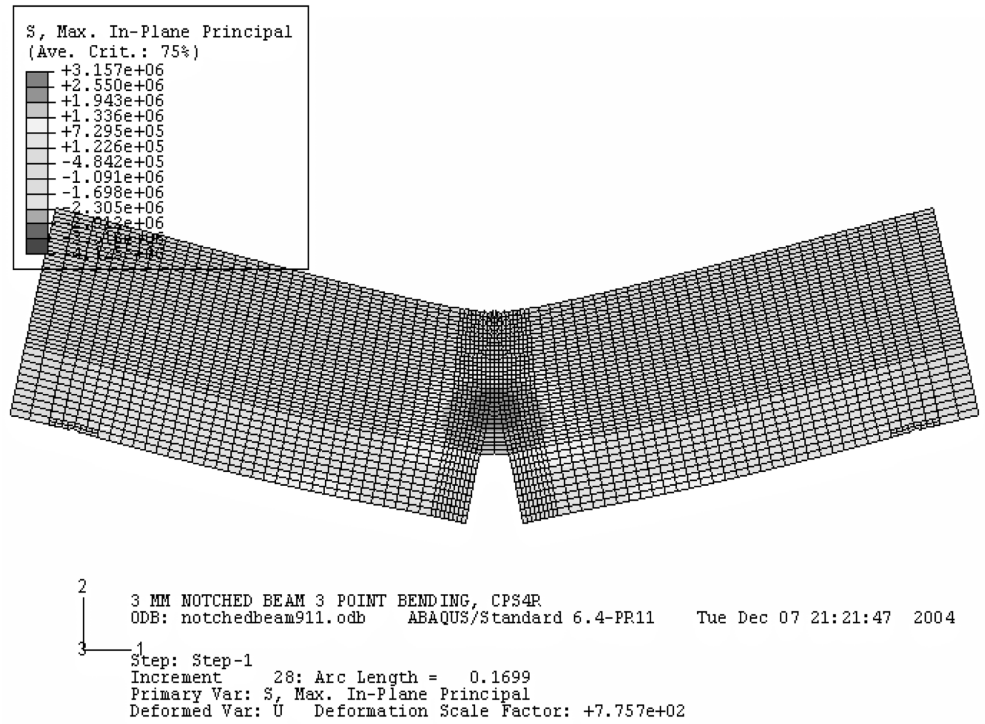

Fig. 7 Cracking deformations and distribution of the maximum principle stress stress under ultimate load

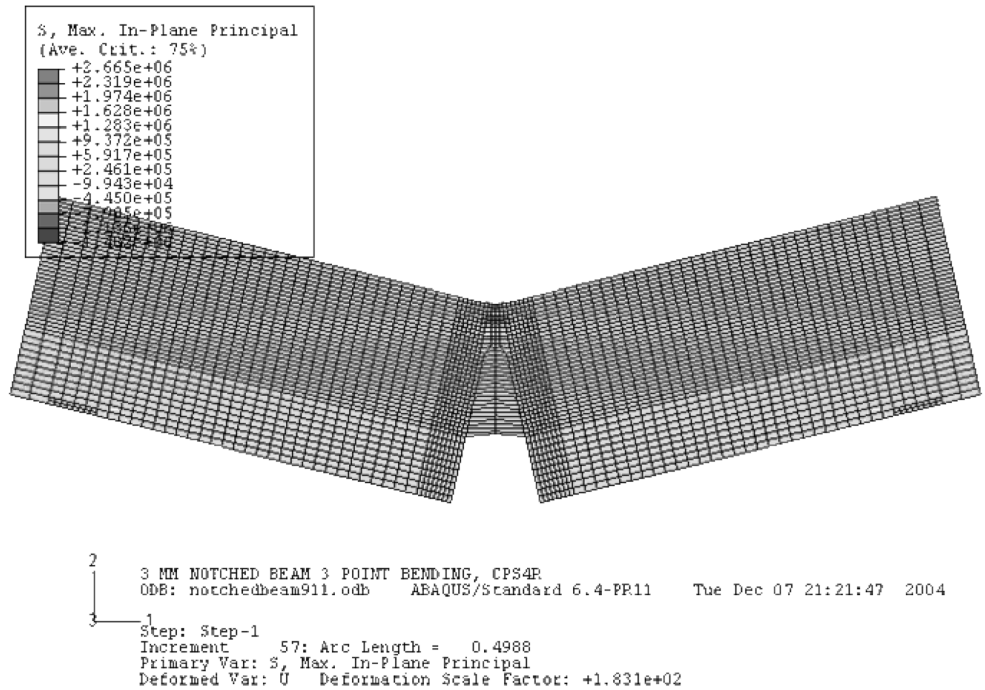

Fig. 8 Ultimate cracking deformations and distribution of the maximum principle stress

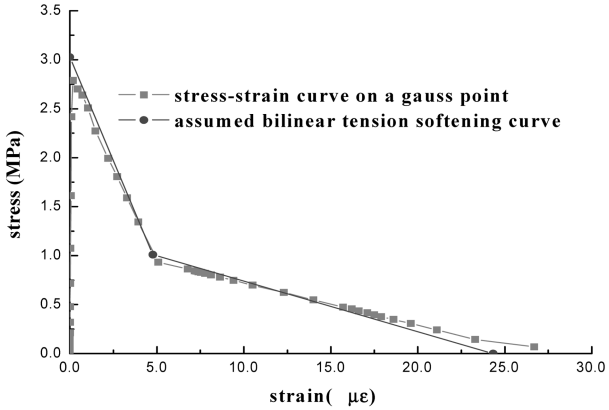

Fig. 9 Stress-strain curve of the first element integral point above the notch

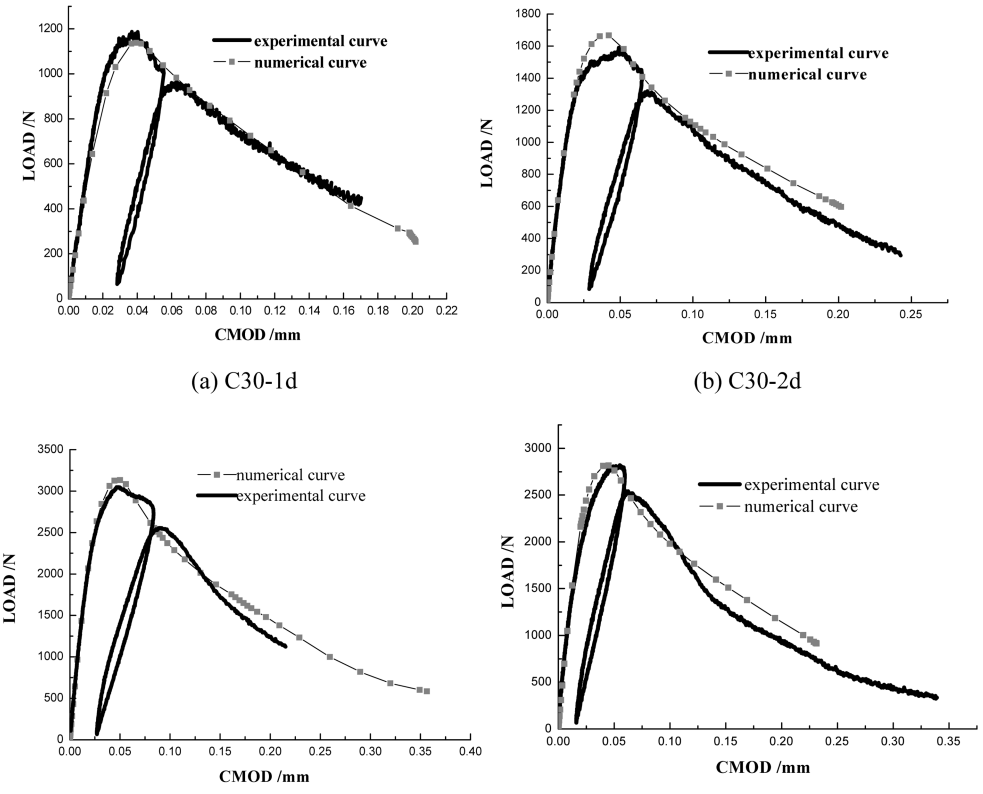

Fig. 10 Comparisons of the simulated LOAD-CMOD curves and the experimental results

shown in Figs. 11~12.

As shown in Figs. 11~12, in the stable crack propagation segment, that is, before the ultimate load, the slope increases with the increment of age. While, in the descending segment, that is, the unstable crack propagation segment, the load rapidly descends with increasing age, especially the

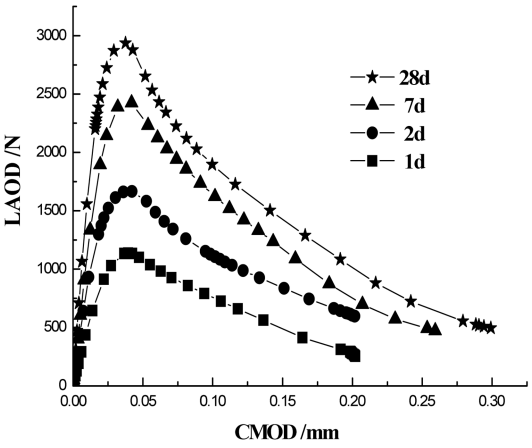

Fig. 11 LOAD-CMOD curves

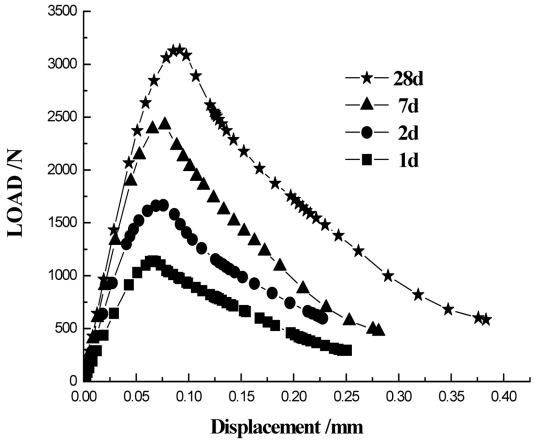

Fig. 12 LOAD-displacement curves

early-age concrete beams. Taking beams of 1d for example, the load descending is relatively slow due to plasticity of young concrete. These conclusions can also be found in the literature of Kim (2004).

The calculations of K_{IC}^{s} and $\mathrm{CTOD_C}$ had been explained in the TPM test, and here another LEFM method will be applied to solve the equivalent elastic critical crack length a_{ce}. Consequently, K_{IC}^{s} and $\mathrm{CTOD_C}$ can be gained by the crack opening displacement (COD) derived from simulations. The detailed processes are listed as follows.

Based on effective-elastic crack approach, for the single side notched three-point bending beams (S=4b), the following equations can be gained:

$$\mathrm{COD}(a,x) = \mathrm{CMOD} \times g_3\left(\frac{a}{D}, \frac{x}{a}\right) \tag{13}$$

$$g_3\left(\frac{a}{D}, \frac{x}{a}\right) = \left\{\left(1-\frac{x}{a}\right)^2 + \left(1.081 - 1.149\frac{a}{D}\right)\left[\frac{x}{a} - \left(\frac{x}{a}\right)^2\right]\right\}^{\frac{1}{2}} \tag{14}$$

where x-the vertical distance away from the bottom of beams
a-length of the crack
g_3-geometry factor

The g_3 function curves for different crack length, a=65, 70, 75, 80, 85 (mm) respectively, are shown in Fig. 13.

Fig. 13 shows that the shape of curves around the crack tip is nonlinear, and as it becomes more distant from the crack tip it shows a linear relationship.

Along the notch, choose five nodes every 10mm from the first node at the bottom of beams, and thus the horizontal displacement of the first node is equal to half the CMOD. With the numerical results, values of COD for five nodes can be obtained when reaching the ultimate load. Then take the CMOD of the first node with any COD of the rest four nodes into the Eq. (13) and a nonlinear equation can be derived about the crack length a. The solution, a, is the equivalent elastic critical

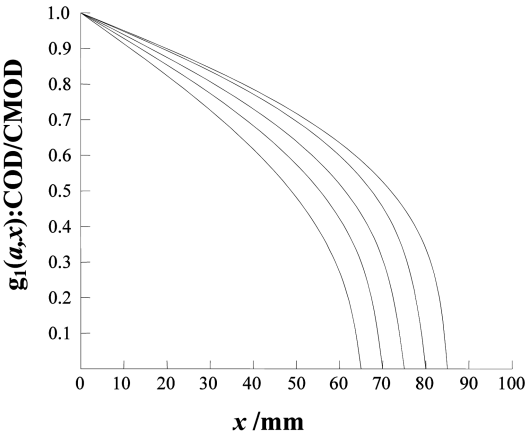

Fig. 13 COD of three-point bending beam (s=4b)

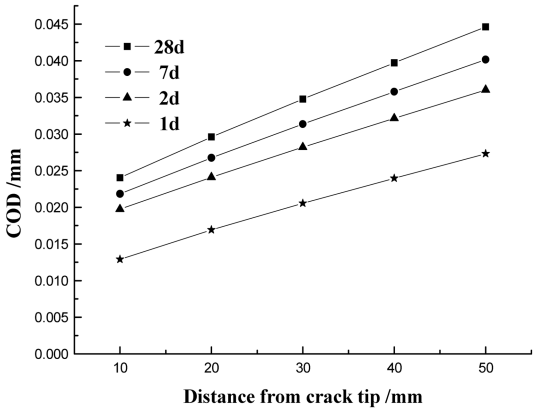

Fig. 14 COD at peak load

crack length, a_{ce}, corresponding to the ultimate load. Then, take another COD into the Eq. (13) and another a_{ce} can be solved the same way. The average value of these two a_{ce} is the final a_{ce}.

Based on effective-elastic crack approach for the three-point bending beams (S=4b), there is:

$$K_{IC}^{s} = \sigma_{\max}\sqrt{\pi a_{ce}}\, g_1\left(\frac{a_{ce}}{D}\right) \tag{15}$$

$$\sigma_{\max} = \frac{3P_{\max}S}{2D^2B} \tag{16}$$

$$g_1\left(\frac{a}{D}\right) = \frac{1.99-(a/D)(1-a/D)[2.15-3.93a/D+2.70(a/D)^2]}{\sqrt{\pi}(1+2a/D)(1-a/D)^{3/2}} \tag{17}$$

Substituting a_{ce} and $P_{\max}$ into the Eq. (17), K_{IC}^{s} can be calculated. Taking a_{ce}, x=50 mm and CMOD into the Eq. (13), $\mathrm{CTOD_C}$ can be obtained.

Taking the concrete beam of one day age as an example, the input data are shown as follows:

$P_{\max}$=1 138N (against experiment result $P_{\max}$ =1 186.7N);

x=0 and CMOD=3.661 28×10^{-2} mm;

x=10 mm and COD=3.240 92×10^{-2} mm;

x=20 mm, COD=2.814 44×10^{-2} mm.

Bring these into the Eq. (13) and solve this nonlinear equation. The results are that:

x=10 mm, a_{ce}=61.18 mm;

x=20 mm, a_{ce}=61.90 mm.

Thus the average value of these two a_{ce} is 61.54 mm. The experiment result of a_{ce} derived from the TPM test is 62.51 mm, and the relative error is 1.6%.

Substituting a_{ce}= 61.54 mm and $P_{\max}$=1 138 N into the Eq. (15) and (16), the K_{IC}^{s} is obtained as 0.325 6 (MPa*m$^{0.5}$) against the experiment result 0.364 5 (MPa*m$^{0.5}$) with the relative error of 10.67%.

Substituting a_{ce}= 61.54 mm, CMOD=3.66×10^{-2}mm, x=50 mm into the Eq. (13), the solved $\mathrm{CTOD_c}$ is 0.0131 mm against the experiment result 0.0117 mm with the relative error of 12.1%. The COD curves under the ultimate load are shown in Fig. 14.

4. Uniaxial tension test

4.1. Preparation of specimens

A total of 12 plate specimens were prepared. The tension specimens were cast in a premade acrylic glass mold with the dimension of 350×100×20 mm. The mold was made of acrylic sheet with a thickness of 25 mm. With such a specimen size, the uniaxial tension can be ensured as a two-dimensional problem.

The further curing of demolded specimens was carried out in a curing room with a temperature of 21±2°C and relative humidity of 100%.

4.2. Experiment program and test results

The setup for the uniaxial tension test is shown in Fig. 15. Two identical loading fixtures were used: one was gripped on the actuator of the MTS machine, the other was connected to the load cell. The loading fixture contained a ball joint that was essential for protecting the tension specimen from possible bending effects. Four aluminum loading plates were glued with the specimen. Then the glued specimen was connected to the loading fixture by using a pin of diameter 12 mm. Four Schaevitz LVDTs (linear variable differential transformer), with a working range of ±0.635 mm and a designed gauge length of 120 mm, were mounted on the two sides of the specimen for deformation measurement as well as test control. The LVDT holders were specially designed to allow the adjustment of the entering and offsetting for the LVDTs.

Tension tests were conducted using a MTS machine with a capacity of 250 kN. The tests were carried out using newly developed adaptive control method (Li, *et al*. 1998). In this method, the control mode could be switched among load cell, MTS stroke displacement, and four LVDTs. The key point for this adaptive control was to use the LVDT that caught the formation of major crack as control. In this way, the loading would gradually decrease with the increase of the LVDT reading.

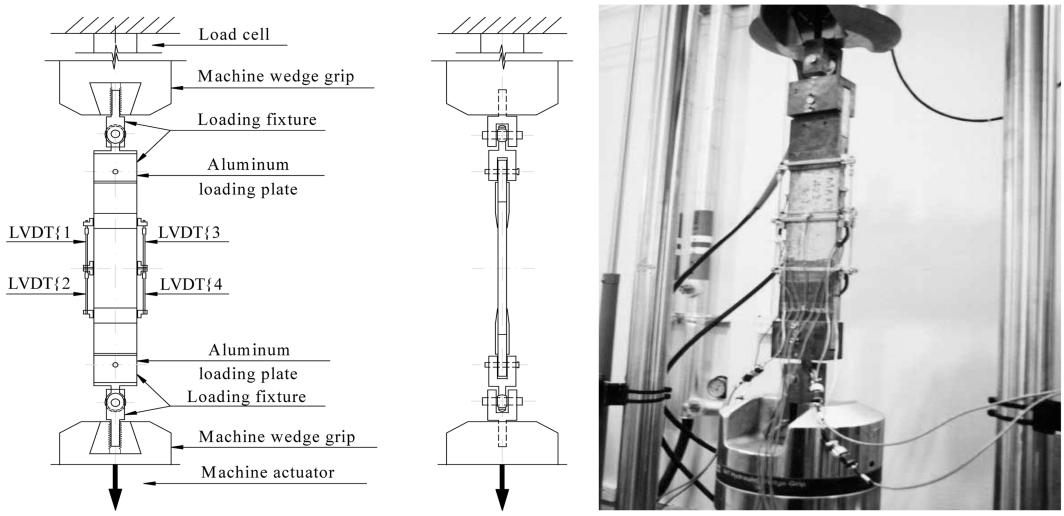

Fig. 15 Uniaxial tension test setup

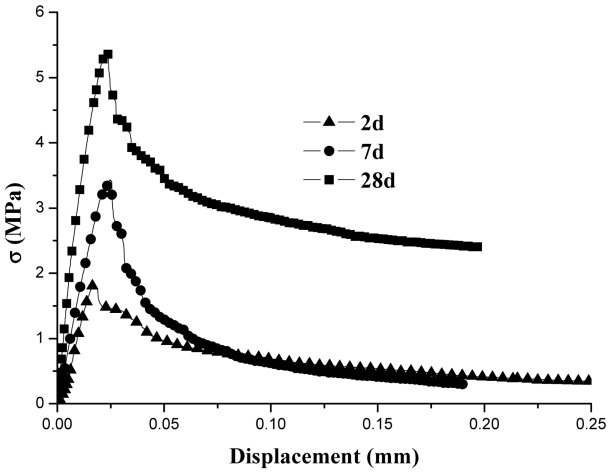

Fig. 16. Stress displacement curves in uniaxial tension

Thus, a stable post-peak response could be measured.

The uniaxial tensile stress-displacement curves obtained in the test are shown in Fig. 16.

In Fig. 16, the increase of the uniaxial tensile strength and initial slope coefficient indicated the development of brittleness with aging which could also be seen from the smooth softening part of the curve at 2 days against the sudden drop after peak load in the curves of 7days and 28 days.

4.3. Damage plastic model

The stress-strain curve under uniaxial tension of damage plastic model for concrete is shown in Fig. 17. From Fig. 17, it can be seen that the curve is linear elastic before peak stress σ_{t0} which indicates the generation of the microcracks. After σ_{t0}, microcracks propagate and expand to macrocracks which lead to the strain localization of concrete specimen which can be shown as the softening part of the curve. It can be concluded from the curve that

$$\varepsilon_{0t}^{el} = \sigma_t / E_0 \tag{18}$$

$$\varepsilon_t^{ck} = \varepsilon_t - \varepsilon_{0t}^{el} \tag{19}$$

$$\sigma_t = (1-d_t)E_0(\varepsilon_t - \varepsilon_t^{pl}) \tag{20}$$

where σ_t is the uniaxial tensile stress; ε_t is the uniaxial tensile strain; E_0 is the initial elastic modulus; ε_{0t}^{el} is the elastic strain neglect damage; ε_t^{ck} is the crack strain of concrete; ε_t^{pl} is the equivalent tensile plastic strain, and d_t is the damage variable of concrete.

The strain softening can be presented by $\sigma_t - \varepsilon_t^{ck}$ curve or $\sigma_t - u_t^{ck}$ curve. As only one main crack generates, the deformation of specimen localizes around the crack zone. Because the deformation of crack zone is independent of the measuring gauge length, the $\sigma_t - u_t^{ck}$ curve in which fracture energy applied is more suitable to present the mechanical properties of strain softening than $\sigma_t - \varepsilon_t^{ck}$ curve. The $\sigma_t - u_t^{ck}$ curve is introduced in this study as $d_t - u_t^{ck}$ well as curve in considering damage effect.

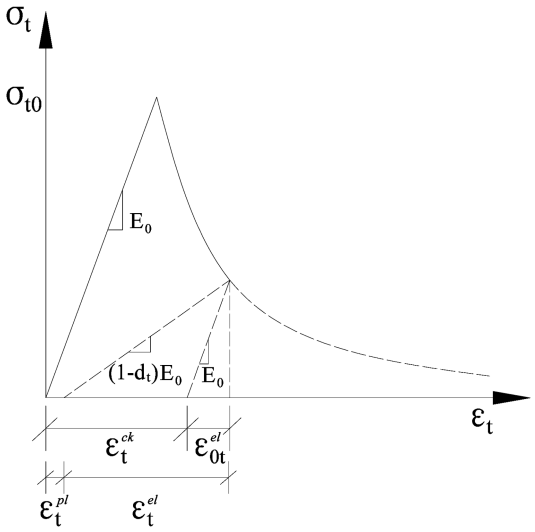

Fig. 17 Stress-strain curve of concrete under uniaxial tension

From Eqs. (18)~(20), it can be seen that the $\sigma_t - u_t^{ck}$ curve and $d_t - u_t^{ck}$ curve can be derived from the damage variable d_t. The unloading curve under uniaxial tension test conducted by Zhao (1996) was applied in this study.

$$\sigma_{td} = \sigma_t - (1.2\sigma_t + 0.09\sigma_{t0})\left[lg\left(\frac{u_t}{u_{td}}\right)\right]^{1/2} \tag{21}$$

where σ_t and u_t are the stress and displacement at unloading point; σ_{td} and u_{td} are the stress and displacement during unloading process, where $\sigma_{td} > 0.1\sigma_{t0}$ and σ_{t0} is peak stress.

Replace the strain in Eqs. (16)~(18) with corresponding displacement, then following expression can be obtained:

$$u_{0t}^{el} = \sigma_t / k_0 \tag{22}$$

$$u_t^{ck} = u_t - u_{0t}^{el} \tag{23}$$

$$\sigma_t = (1 - d_t)k_0(u_t - u_t^{pl}) \tag{24}$$

where u_t is the uniaxial tensile displacement; k_0 is the initial slope coefficient of the linear part in stress-displacement curve; u_{0t}^{el} is the elastic displacement neglect damage; u_t^{ck} is the crack displacement of concrete; u_t^{pl} is the equivalent tensile plastic displacement.

With the stress and displacement at unloading point (σ_t, u_t) and $\sigma_{td} = 0$, in Eq. (21), the residual displacement u_{td} can be calculated as the equivalent tensile plastic displacement u_t^{pl}. Substituting (σ_t, u_t) and u_t^{pl} into Eq. (24), the damage variable d_t can be derived. With the crack displacement u_t^{ck} obtained from Eq. (22) and Eq. (23), the $\sigma_t - u_t^{ck}$ curve and $d_t - u_t^{ck}$ curve are finally determined. The whole process, as shown in Fig. 18, is programmed to simulate the uniaxial tension test of concrete by ABAQUS in damage plastic model.

Taking concrete at 28d as example, with the carefully selected stress and displacement, (σ_t, u_t), at tension softening curve derived from experiment, the $\sigma_t - u_t^{ck}$ curve and $d_t - u_t^{ck}$

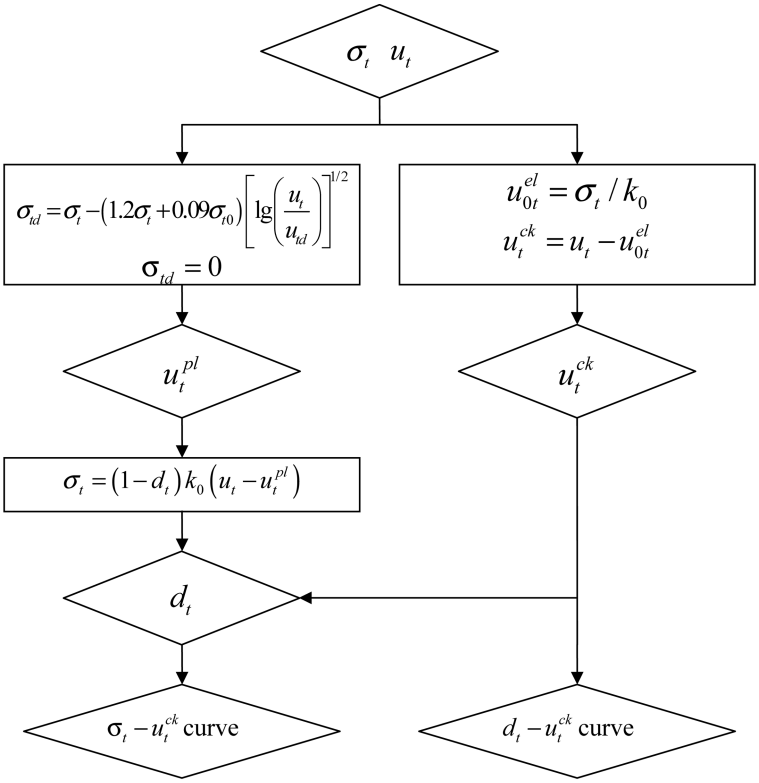

Fig. 18 Flow chart of the numerical procedure

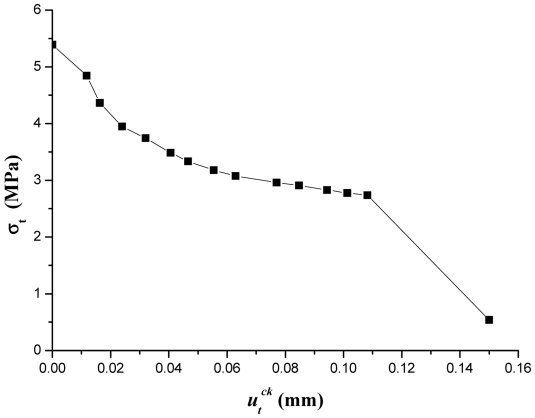

Fig. 19 $\sigma_t - u_t^{ck}$ curve

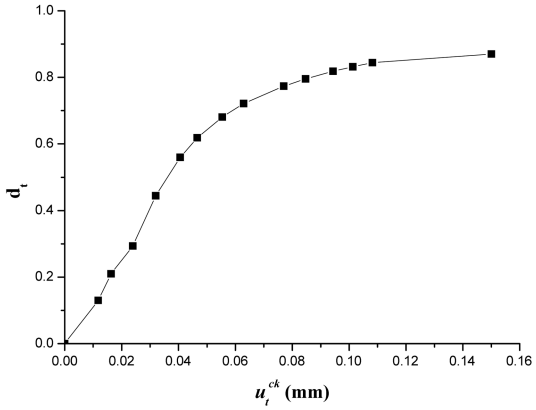

Fig. 20 $d_t - u_t^{ck}$ curve

curve, as shown in Fig. 19 and Fig. 20, are configured.

4.4. Numerical simulation

4.4.1. Finite element modeling and detailed gridding mesh

As shown in Fig. 21, a tie constraint in ABAQUS was applied to simulate the contact face

between concrete specimen and aluminum loading plate as well as the contact face between aluminum loading plate and loading fixture against relative slipping. With kinematic coupling constraint in ABAQUS, all the nodes on the aluminum loading plate were coupled to a reference node to which the constraint and load was applied to control the movement and deformation of the specimen. The linear elastic constitutive relationship was employed in materials of loading fixture and aluminum loading plate.

In this analysis, C3D8R elements in ABAQUS were applied. One end of the model was fixed, while the displacement was loaded on the reference point at the other end. With the modified Riks method, the complete stress-strain curves were derived.

Still, a series meshing model were made actually and the numerical results were almost the same.

4.4.2. Numerical analysis

Base on the research of Lublinerm, the crack generates when the equivalent tensile plastic strain $\varepsilon_t^{pl} > 0$ and the value and direction of the maximum plastic principle strain is positive and vertical to crack, respectively. So, once plotted the vector diagram of the maximum principle plastic strain, the whole failure process of microcracks propagated to macrocracks in uniaxial tension test is pictured clearly. In Fig. 22, the maximum principal plastic strain is displayed as vector arrows along the specimen at a certain step and at failure.

As shown in Fig. 22, at a certain step, the arrows mostly centralized in the middle of the specimen against the scattered vector arrows at the other parts which meant the generation and propagation of the microcracks in the middle of the specimen. At failure, because only one main

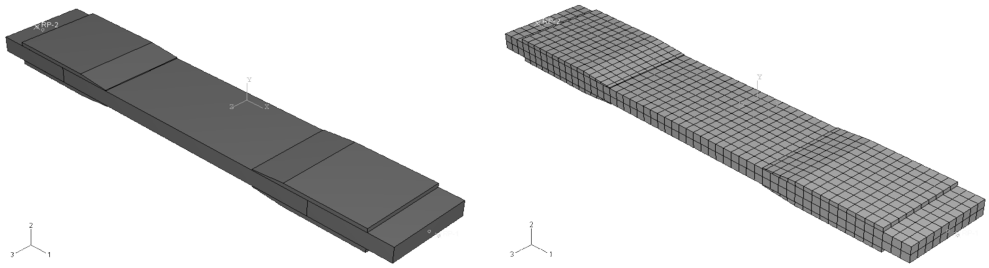

(a) Finite element model (b) Detailed gridding mesh

Fig. 21 Finite element model and detailed gridding mesh

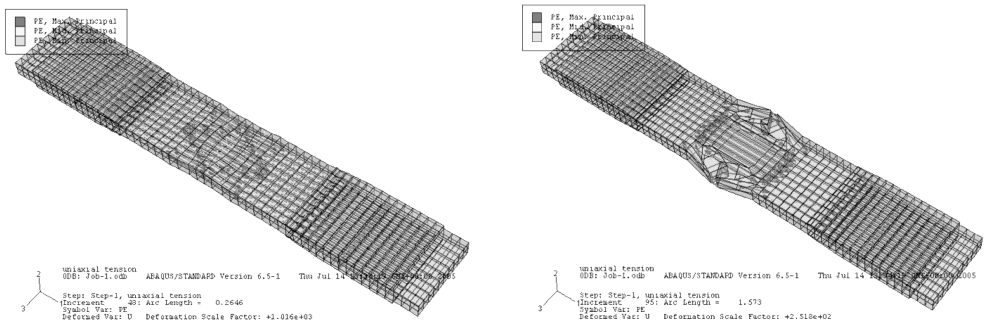

(a) at a certain step (b) at failure

Fig. 22 Maximum principal plastic stain

macrocrack generates, so all the arrows concentrate in the middle of the specimen.

The damage of concrete specimen at a certain step and at failure was shown in Fig. 23.

As shown in Fig. 24, the principal stress evenly distributes along the width of the concrete specimen at the connected part between two aluminum loading plates. Thus, it can be concluded that the eccentric bending has little influence in loading process.

The numerical complete stress-displacement curves and experimental curves at ages of 2, 7 and 28 days are shown in Figs. 25~27.

As shown in Figs. 25~27, the numerical simulated results had a good agreement with the experimental results. The main difference between numerical results and experimental results came from the unavoidable energy loss and experimental error.

5. Conclusions

The following conclusions can be drawn from the current research:

In numerical simulation of three-point bending test of this research, smear crack model with bilinear softening curves was applied to obtain fracture parameters. The simulated results were very close to the results obtained by TPM. It implied that there may be some relations between two-parameter model and smeared cracking model. A further investigation is needed to confirm the observation.

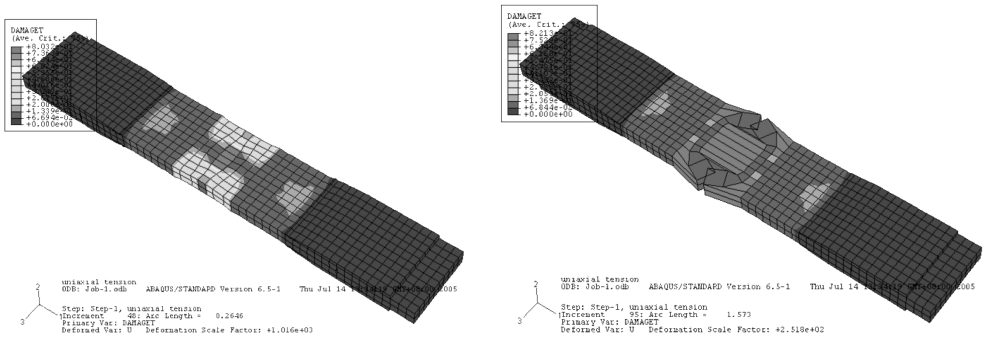

(a) at a certain step (b) at failure

Fig. 23 Damage of the specimen

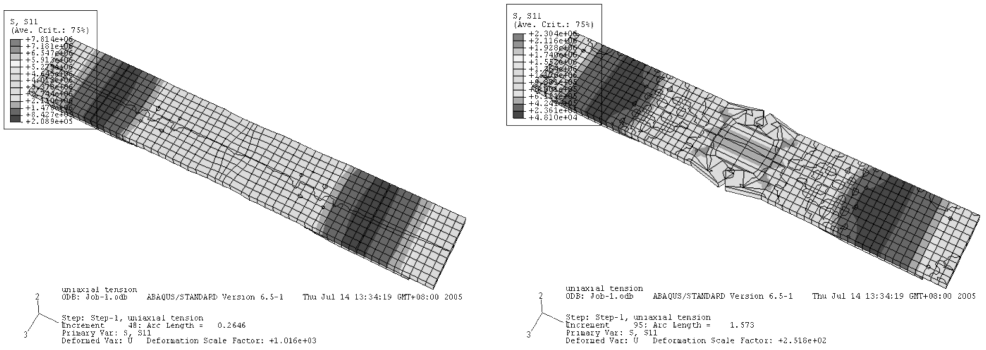

(a) at a certain step (b) at failure

Fig. 24 Principal stress profile in 2 direction

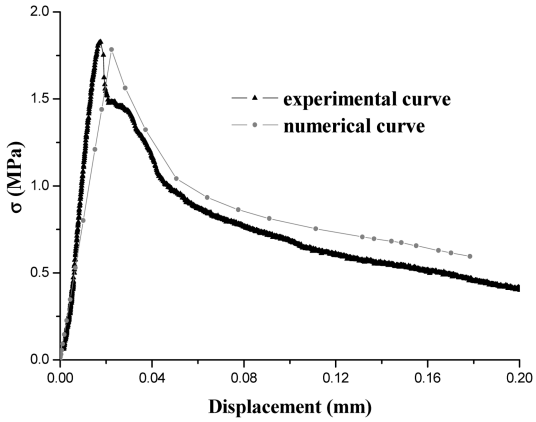

Fig. 25 Stress-displacement curve at 2 day

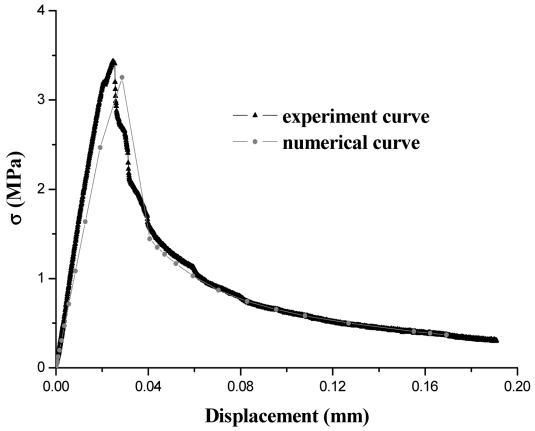

Fig. 26 Stress-displacement curve at 7 day

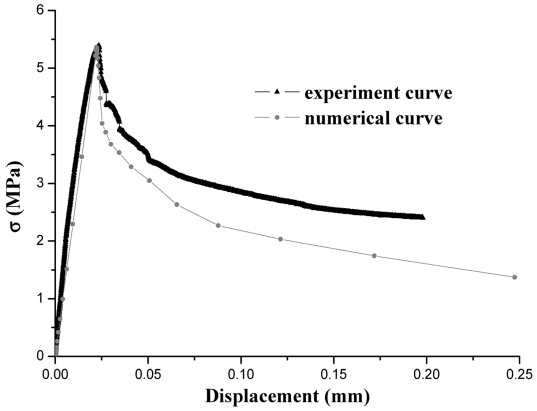

Fig. 27 Stress-displacement curve at 28 day

In simulating the uniaxial tension test, the damage plastic model and smeared crack model were incorporated into the numerical analysis. In this way, the damage and fracture process could be analyzed numerically in one program to interpret the properties of concrete at different ages.

All the simulated results agreed well with the experimental results of concretes at different ages, including the LOAD-CMOD curves under three point bending and the complete stress-displacement curves under uniaxial tension. The development of the properties of concrete at different ages confirmed to the relevant experiment results.

Notation

There-Point Bending Test

a length of the crack

a_0 depth of the notch

a_{ce} equivalent elastic c critical crack length

a_e critical effective crack length

B	width of the beam
C_i	initial flexibility
C_u	unloading flexibility
CMOD	crack mouth opening displacement
COD	crack opening displacement
$CTOD_C$	critical crack tip opening displacement
D	depth of the three-point bending beam
E	modulus of elasticity
E_0	initial modulus of elasticity
F, V	shape function
g_1, g_3	geometry factors
G_0	initial modulus of shear
G_F	energy required to develop an unit area crack
G_f^s	area under the initial slope
G_{IC}^s	critical strain energy release rate
H_0	thickness of the clamp
$k_{softl,1}$	tension crack softening coefficient of crack 1
$k_{softl,2}$	tension crack softening coefficient of crack 2
K_{IC}^s	critical stress intensity factor
L	length of the beam
LEFM	linear elastic fracture mechanics
P_{max}	ultimate load
S	span length
TPM	two-parameter model
W	weight of the beam
x	vertical distance away from the bottom of beams
σ_{nn}	positive stress of crack 1
σ_{tt}	positive stress of crack 2
σ_{nt}	shear stress
ε_{nn}	positive strain of crack 1
ε_{tt}	positive strain of crack 2
ε_{nt}	shear strain
φ	shear transfer factor

Uniaxial Tension Test

d_t	damage variable of concrete
k_0	initial slope coefficient of the linear part in stress-displacement curve
u_t	uniaxial tensile displacement
u_{td}	displacement during unloading process
u_{0t}^{el}	elastic displacement neglect damage
u_t^{ck}	crack displacement of concrete
u_t^{pl}	equivalent tensile plastic displacement
σ_t	uniaxial tensile stress

σ_{t0} peak stress
σ_{td} stress during unloading process
ε_t uniaxial tensile strain
ε_{0t}^{el} elastic strain neglect damage
ε_t^{ck} crack strain of concrete
ε_t^{pl} equivalent tensile plastic strain

Acknowledgements

The financial support of the National Natural Science Foundation of China (NSFC50578142) is greatly acknowledged.

Refrences

Bazant, Z. P. (2002), "Concrete fracture models: testing and practice", *Eng. Fract. Mech.*, **69**(2), 165-205.
Bazant, Z. P. and Becq-Giraudon, E. (2002), "Statistical prediction of fracture parameters of concrete and comparison of testing methods", *Cement Concrete Res.*, **32**(4), 529-556 APR 2002.
Bazant, Z. P. and Emilie, B.-G. (2002), "Statistical prediction of fracture parameters of concrete and implications for choice of testing standard", *Cement Concrete Res.*, **32**(4), 529-556.
Bazant, Z. P. and Planas, J. (1997), *Fracture and Size Effect in Concrete and Other Quasibrittle Materials*, Boca Baton, CRC Press.
De, G., Schutter, M. and Vuylsteke (2004), "Minimisation of early age thermal cracking in a J-shaped non-reinforced massive concrete quay wall", *Eng. Struct.*, **26**(6), 801-808.
Guinea, G. V. and Elices, M. and Planas, J. (1997), "On the initial shape of the softening function of cohesive materials", *J. Int J. Fract*, **87**(1), 49-139.
Guinea, G. V., Planas. J. and Elices, M. (1994), "A general bilinear fit for the softening curve of concrete", *J. Mater. Struct.*, **27**(1), 99-105.
Hanson, J. H. and Ingraffea A. R. (2003), "Using numerical simulations to compare the fracture toughness values for concrete from the size-effect, two-parameter and fictitious crack models", *Eng. Fract. Mech.*, **70**, 1015-1027.
Hillerborg, A., Modéer, M. and Petersson, P.-E. (1976), "Analysis of crack formation and crack growth in concrete by means of fracture mechanics and finite elements", *Cement Concrete Res.*, **6**(6), November 1976, 773-781.
Jenq, Y. S. and Shah, S. P. (1985), "Two parameter fracture model for concrete", *J. Eng. Mech.*, **111**(10), 1227-1241.
Jin, X. Y., Jin, N. U. and Jin, X. (2004), "KIC and CTODC of young concrete", *8th International Symposium on Structural Engineering for Young,* 2004.8.
Jin, X. Y., Shen, Y., and Li, Z. J. (2005), "Behavior of high and normal strength concrete at early ages", *Mag. Conc. Res.*, **57**(6), 339-345.
Kim, J.-K., Lee, Y. and Yi, S.-T. (2004), "Fracture characteristics of concrete at early ages", *Cement Concrete Res.*, **34**, 507-519.
Li, Z. J. and Xianyu, J. (2004), "Investigation on relationship of prostity and fracture parameter of concrete at early-age", *IntegratedLife-Cycle Management of Infrastructures*, 2004. 11, pp85-91, Hong Kong, China.
Niu, Y. Z., Chuanlin, T., Liang, R. Y. and Shuiwen, Z. (1995), "Modeling of thermomechanical damage of early-age concrete", *J. Struct. Eng.*, ASCE, **121**(4), 1995, 717-726.
Oestergaard, L., Lange, D.A. and Stang, H. (2004), "Early-age stress-crack opening relationships for high

performance concrete", *Cement Concrete Compos.*, **26**(5), 563-572.
Petersson, P. E. (1981), "Crack growth and development of fracture zones in plain concrete and similar materials", Report No. TVBM-1006, *Division of Building materials*, Lund Institute of Technology, Lund, Sweden, 1981.
Planas, J., Elices, M. and Guinea, G. V. (1992), "Measurement of the fracture energy using three-point bend test: Part2-Influence of bulk energy dissipation", *J. Mater. Struct*, **25**(4), 12-305.
Roman Lackner, Herbert A. Mang (2004), "Chemoplastic material model for the simulation of early-age cracking: From the constitutive law to numerical analyses of massive concrete structures", *Cement Concrete Compos.*, **26**(5), 551-562.
Shang, Renjie, Zhao, Guofan and Huang, Chengkui (1996), "Experimental investigation of complete stress-deformation curves for concrete under low frequency cyclic load", *J. Hydraulic Eng.*, **7**, 82-87.

CC